

High-resolution viscous terms discretization and ILW solid wall boundary treatment for the Navier–Stokes equations

Rafael B. de Rezende Borges · Nicholas Dicati P. da Silva · Francisco A. Gomes · Chi-Wang Shu

Received: date / Accepted: date

Abstract Robust numerical methods for CFD applications, such as WENO schemes, quickly evolved in the past few decades. Together with the Inverse Lax–Wendroff (ILW) procedure, WENO ideas were also applied in the boundary treatment. Those methods are known for their high-resolution property, i.e., good representation of nonlinear phenomena, which is an important property in solving challenging engineering problems. In light of that, the objective of this work is to present a review of well-established high-resolution numerical methods to solve the Euler equations and adapt the Navier–Stokes viscous terms discretization and boundary treatment. To test the modifications, we employed the positivity-preserving Lax–Friedrichs splitting, multi-resolution WENO scheme, third-order strong stability preserving Runge–Kutta time discretization,

The research of C.-W. Shu is partly supported by AFOSR grant FA9550-20-1-0055 and NSF grant DMS-2010107.

Rafael B. de Rezende Borges
Rio de Janeiro State University, Mathematics and Statistics Institute, Rio de Janeiro, Brazil
<https://orcid.org/0000-0002-2576-8118>
E-mail: rafael.borges@ime.uerj.br

Nicholas Dicati P. da Silva
Maringá State University, Department of Mechanical Engineering, Maringá, Brazil
<https://orcid.org/0000-0002-5808-3932>
E-mail: ndicati@gmail.com

Francisco A. A. Gomes
Federal University of Technology - Paraná, Department of Mechanical Engineering, Pato Branco, Brazil
<https://orcid.org/0000-0001-6204-1439>
E-mail: franciscogomes@utfpr.edu.br

Chi-Wang Shu
Brown University, Division of Applied Mathematics, Providence, United States of America
E-mail: chi-wang.shu@brown.edu

and ILW boundary treatment. The first problems were simple flows with analytical solutions for accuracy tests. We also tested the accuracy with nontrivial phenomena in the vortex flow. Oblique shock and complicated flow structures were captured in the Rayleigh–Taylor instability and flow past a cylinder. We showed the discretization and boundary treatment can handle non-constant viscosity, are high-order, high-resolution, and behaves similarly to the well-established numerical methods. Furthermore, the methods discussed here can preserve symmetry and no approximations regarding the boundary layer were made. Therefore, the discretization and boundary treatment can be considered when solving direct numerical simulations.

Keywords Compressible · Navier–Stokes · Discretization · Inverse Lax–Wendroff · Solid wall · Multi-resolution WENO

1 Introduction

High-order and high-resolution numerical methods quickly evolved in the past few decades, either in the interior scheme or at the boundaries [1–5]. WENO is a robust class of schemes known for their high-resolution property and is popular for solving CFD problems with nonlinear phenomena and complex flow structures [6–8,3]. Stall in aerodynamic profiles or turbomachinery blades, flow separation, side loads, mixing, combustion, and detonation are examples of challenging engineering problems that demand robust numerical solvers [9–16]. Moreover, LES and DNS computations are becoming more feasible and require restricted time and space scales, which can be attained through high-resolution methods [17–19].

Depending on the phenomena, one may need three-dimensional discretization, compressibility and viscous effects, small grid sizes, and small time steps [18, 17, 13]. The Euler equations can be used, e.g., to solve compressible fluid flows containing shock waves. However, it will not be able to model the boundary layer and related phenomena. By adding viscous terms to the Euler equations, one reaches the so-called Navier–Stokes equations, which are capable of modeling challenging engineering problems.

When solving the Navier–Stokes equations, a boundary layer will develop near solid walls. The boundary layer or the turbulent flow near the wall has a great impact in academical and industrial applications [20]. To maintain the interior scheme high-resolution, the boundary conditions shall be properly imposed at the walls. Among the boundary imposition strategies, the Inverse Lax–Wendroff (ILW) is distinguished by its ability to be applied to rectangular meshes on arbitrary domains, easing the mesh construction and spatial discretization [21, 2, 22, 5].

While reviewing well-established numerical methods to solve the Euler equations, we will present modifications to add the viscous contribution and we will introduce a new way of discretizing the first-order derivatives of the viscous terms using already-available information from the inviscid fluxes. Moreover, we will show how to adapt the ILW boundary condition imposition at solid walls without using rotation, something that has not been experimented before in the literature for the Navier–Stokes equations. This is found in Section 2.2.

To assess these modifications, in Section 3 we will solve simple 2D flows, as well as the vortex flow, the Rayleigh–Taylor instability, and the supersonic flow past a cylinder. To do that, we will employ the positivity-preserving Lax–Friedrichs splitting [1], multi-resolution central WENO [8], WENO-type extrapolation [21], and Inverse Lax–Wendroff boundary (ILW) treatment [21, 2, 5, 22].

2 Numerical Methods

2.1 Discretization

In this paper, we are interested in the following set of equations

$$\mathbf{U}_t + \mathbf{F}(\mathbf{U})_x + \mathbf{G}(\mathbf{U})_y = \mathbf{S}_{1x} + \mathbf{S}_{2y} + \mathbf{S}(\mathbf{U}), \quad (1)$$

where

$$\mathbf{U} = \begin{bmatrix} \rho \\ \rho u \\ \rho v \\ E \end{bmatrix}, \quad \mathbf{F}(\mathbf{U}) = \begin{bmatrix} \rho u \\ \rho u^2 + p \\ \rho uv \\ u(E + p) \end{bmatrix}, \quad (2)$$

$$\mathbf{G}(\mathbf{U}) = \begin{bmatrix} \rho v \\ \rho uv \\ \rho v^2 + p \\ v(E + p) \end{bmatrix}, \quad \mathbf{S}_1 = \begin{bmatrix} 0 \\ \tau_{xx} \\ \tau_{xy} \\ \epsilon_{vx} + \frac{\mu}{Pr(\gamma - 1)} \frac{\partial(a^2)}{\partial x} \end{bmatrix}, \quad (3)$$

$$\mathbf{S}_2 = \begin{bmatrix} 0 \\ \tau_{xy} \\ \tau_{yy} \\ \epsilon_{vy} + \frac{\mu}{Pr(\gamma - 1)} \frac{\partial(a^2)}{\partial y} \end{bmatrix}, \quad (4)$$

the source term $\mathbf{S}(\mathbf{U})$ depends on the problem, and ρ , u , v , and p are the density, x and y velocities, and pressure, respectively. E , τ , ϵ_v , and a are the the total energy per unit of volume, viscous tensor, viscous dissipation rate, and speed of sound, respectively, given as

$$E = \frac{p}{\gamma - 1} + \frac{\rho}{2}(u^2 + v^2), \quad \tau_{xx} = \mu \left(\frac{4}{3} \frac{\partial u}{\partial x} - \frac{2}{3} \frac{\partial v}{\partial y} \right) \quad (5)$$

$$\tau_{xy} = \mu \left(\frac{\partial u}{\partial y} + \frac{\partial v}{\partial x} \right), \quad \tau_{yy} = \mu \left(\frac{4}{3} \frac{\partial v}{\partial y} - \frac{2}{3} \frac{\partial u}{\partial x} \right) \quad (6)$$

$$\epsilon_{vx} = u\tau_{xx} + v\tau_{xy}, \quad \epsilon_{vy} = u\tau_{xy} + v\tau_{yy}, \quad a = \sqrt{\frac{\gamma p}{\rho}}, \quad (7)$$

where $\gamma = 1.4$, $\mu = 5 \cdot 10^{-5} \text{ Pa} \cdot \text{s}$, and $Pr = 0.7$ are the specific heat ratio, absolute viscosity, and the Prandtl number for the air, respectively. Unless explicitly stated, these properties will be used in the test problems.

We discretize the fluxes \mathbf{F} and \mathbf{G} with the following conservative finite difference scheme [23]:

$$\frac{d\mathbf{U}_{i,j}(t)}{dt} = -\frac{1}{\Delta x} \left(\hat{\mathbf{F}}_{i+1/2,j} - \hat{\mathbf{F}}_{i-1/2,j} \right) - \frac{1}{\Delta y} \left(\hat{\mathbf{G}}_{i,j+1/2} - \hat{\mathbf{G}}_{i,j-1/2} \right), \quad (8)$$

where $\Delta x = \Delta y = \text{constant}$ is the mesh size.

To compute the numerical flux, we use the positivity-preserving Lax–Friedrichs splitting [1]

$$\mathbf{F}^\pm(\mathbf{U}_{i,j}) = \frac{1}{2} \left(\mathbf{U}_{i,j} \pm \frac{\mathbf{F}(\mathbf{U}_{i,j})}{\alpha_x} \right), \quad (9)$$

where $\alpha_x = \max_U \max_m |\lambda_m(\mathbf{U})|$ is computed for the whole domain [23], λ_m are the eigenvalues of the Jacobian, and $m = 1, \dots, 4$ is the m -th vector component.

Through a local characteristic decomposition, we have

$$\mathbf{H}_\pm = \mathbf{L}(\mathbf{U}_{i+1/2,j}) \mathbf{F}^\pm(\mathbf{U}_{i,j}), \quad (10)$$

where $\mathbf{U}_{i+1/2,j} = (\mathbf{U}_{i,j} + \mathbf{U}_{i+1,j})/2$ is an average state and \mathbf{L} is the left eigenvector.

As in [1], we approximate $(\mathbf{H}_+)_\pm^{i+1/2,j}$ with \mathbf{H}_+ and a multi-resolution WENO reconstruction. The same is valid for $(\mathbf{H}_-)_\pm^{i+1/2,j}$ with \mathbf{H}_- . Then, we transform back with the right eigenvector, \mathbf{R} ,

$$\begin{aligned} (\mathbf{F}_+)_\pm^{i+1/2,j} &= \mathbf{R}(\mathbf{U}_{i+1/2,j}) (\mathbf{H}_\pm)_\pm^{i+1/2}, \\ (\mathbf{F}_-)_\pm^{i+1/2,j} &= \mathbf{R}(\mathbf{U}_{i+1/2,j}) (\mathbf{H}_\pm)_\pm^{i+1/2}, \end{aligned} \quad (11)$$

and form the numerical flux [1]

$$\hat{\mathbf{F}}_{i+1/2,j} = \alpha_x \left[(\mathbf{F}_+)_\pm^{i+1/2,j} - (\mathbf{F}_-)_\pm^{i+1/2,j} \right]. \quad (12)$$

We remark that the procedure is analogous for the \mathbf{G} flux. Among other choices, the multi-resolution WENO of [4,8] can reach machine error for steady non-smooth problems and preserve symmetry. Symmetry breaking issues are addressed, e.g., in [3,24]. We compute the reconstruction polynomials for a fixed j with $r = -s, \dots, s$, $s = 1, \dots, 3$, [4,23]

$$q_1(\xi) = h_{i,j}, \quad (13)$$

and

$$\int_r^{r+1} q_{s+1}(\xi) d\xi = h_{i+r,j}. \quad (14)$$

Next, we obtain equivalent expressions for the reconstruction polynomials [4]

$$p_1(\xi) = q_1(\xi), \quad p_r(\xi) = \frac{q_r(\xi)}{\Gamma_{r,r}} - \sum_{s=1}^{r-1} \frac{\Gamma_{s,r}}{\Gamma_{r,r}} p_s(\xi), \quad (15)$$

with $s = 1, \dots, r$, $r = 2, \dots, 3$, and

$$\Gamma_{s,r} = \frac{\bar{\Gamma}_{s,r}}{\sum_{l=1}^r \bar{\Gamma}_{l,r}}, \quad \bar{\Gamma}_{s,r} = 10^{s-1}. \quad (16)$$

The smoothness indicators are obtained through [4, 8]:

$$\beta_r = \sum_{\alpha=1}^{2(r-1)} \int_0^1 \left[\frac{d^\alpha p_r(\xi)}{d\xi^\alpha} \right]^2 d\xi, \quad r = 2, \dots, 3, \quad (17)$$

$$\varsigma_0 = (h_{i,j} - h_{i-1,j})^2, \quad \varsigma_1 = (h_{i+1,j} - h_{i,j})^2, \quad (18)$$

$$\bar{\Gamma}_{0,1} = \begin{cases} 1 & \varsigma_0 \geq \varsigma_1 \\ 10 & \text{otherwise} \end{cases}, \quad \bar{\Gamma}_{1,1} = 11 - \bar{\Gamma}_{0,1}, \quad (19)$$

$$\Gamma_{0,1} = \frac{\bar{\Gamma}_{0,1}}{\bar{\Gamma}_{0,1} + \bar{\Gamma}_{1,1}}, \quad \Gamma_{1,1} = 1 - \Gamma_{0,1},$$

$$\sigma_0 = \Gamma_{0,1} \left(1 + \frac{|\varsigma_0 - \varsigma_1|^2}{\varsigma_0 + \epsilon} \right), \quad (20)$$

$$\sigma_1 = \Gamma_{1,1} \left(1 + \frac{|\varsigma_0 - \varsigma_1|^2}{\varsigma_1 + \epsilon} \right), \quad \sigma = \sigma_0 + \sigma_1,$$

$$\beta_1 = \frac{1}{\sigma^2} [\sigma_0(h_{i,j} - h_{i-1,j}) + \sigma_1(h_{i+1,j} - h_{i,j})]^2. \quad (21)$$

The nonlinear weights are [4,7]:

$$\omega_r = \frac{\alpha_r}{\sum_{s=1}^3 \alpha_s}, \quad (22)$$

$$\alpha_r = \Gamma_{r,3} \left[1 + \left(\frac{\tau}{\beta_r + 10^{-6}} \right) \right], \quad (23)$$

$$\tau = \left(\frac{\sum_{s=1}^2 |\beta_3 - \beta_s|}{2} \right)^2. \quad (24)$$

Finally, the multi-resolution WENO reconstruction is

$$h_{i+1/2,j}^- = \sum_{r=1}^3 \omega_r p_r(1). \quad (25)$$

The reconstruction for a fixed i is analogous. For the viscous terms, \mathbf{S}_1 and \mathbf{S}_2 , we have the advantage of $(\mathbf{F}_\pm)_\pm^{i+1/2,j}$ being already computed. Therefore, we use the numerical flux approximation regarding the flux splitting (9),

$$\hat{\mathbf{U}}_{i+1/2,j} = (\mathbf{F}_+)_\pm^{i+1/2,j} + (\mathbf{F}_-)_\pm^{i+1/2,j}. \quad (26)$$

Then,

$$\begin{aligned} (\mathbf{U}_x)_{i,j} &= \frac{1}{\Delta x} (\hat{\mathbf{U}}_{i+1/2,j} - \hat{\mathbf{U}}_{i-1/2,j}), \\ \frac{\partial \mathbf{W}}{\partial \mathbf{U}} &= \begin{bmatrix} 1 & 0 & 0 & 0 \\ -u/\rho & 1/\rho & 0 & 0 \\ -v/\rho & 0 & 1/\rho & 0 \\ \frac{1}{2}(\gamma-1)(u^2+v^2) & (1-\gamma)u & (1-\gamma)v & \gamma-1 \end{bmatrix}, \end{aligned} \quad (27)$$

$$(\mathbf{W}_x)_{i,j} = \frac{\partial \mathbf{W}}{\partial \mathbf{U}} (\mathbf{U}_x)_{i,j}. \quad (28)$$

Using the same procedure for the y -direction derivatives, we can compute \mathbf{S}_1 and \mathbf{S}_2 . The viscous terms derivatives are then approximated with a central fourth-order discretization, e.g.,

$$(\mathbf{S}_{1x})_{i,j} = \frac{\mathbf{S}_{1i-2,j} - 8\mathbf{S}_{1i-1,j} + 8\mathbf{S}_{1i+1,j} - \mathbf{S}_{1i+2,j}}{12\Delta x}. \quad (29)$$

One should notice that this will demand approximations to \mathbf{S}_1 and \mathbf{S}_2 at the ghost points.

Once the spatial approximation, $L(\mathbf{U})$, is computed for all interior points, we use the third-order SSP Runge–Kutta to integrate from time step n to $n + 1$ [23]:

$$U_m^{(1)} = U_m^n + \Delta t L(U_m^n), \quad (30)$$

$$U_m^{(2)} = \frac{3}{4}U_m^n + \frac{1}{4}U_m^{(1)} + \frac{1}{4}\Delta t L(U_m^{(1)}), \quad (31)$$

$$U_m^{n+1} = \frac{1}{3}U_m^n + \frac{2}{3}U_m^{(2)} + \frac{2}{3}\Delta t L(U_m^{(2)}). \quad (32)$$

The time step, Δt , can be computed as [2] ($\Delta = \min(\Delta x, \Delta y)$):

$$\Delta t = \min \left[\frac{CFL}{\frac{\alpha_x}{\Delta x} + \frac{\alpha_y}{\Delta y} + \frac{6\alpha_d(\Delta x^2 + \Delta y^2)}{\Delta x^2 \Delta y^2}}, \Delta^{5/3} \right], \quad (33)$$

where α_x and α_y are the same as in (9) for the x - and y -direction, and α_d is the absolute largest eigenvalue for the diffusive terms.

2.2 Boundary Conditions

The boundary conditions will be handled with the ILW procedure regarding [2, 5, 21, 22]. We use the 1D WENO-type extrapolation of [21]. Here, we present a generic coordinate, η , and construct polynomial approximations, $p(\eta)$, for each one of the five candidate substencils

$$S_r = \{\eta_0, \dots, \eta_r\}, \quad r = 0, \dots, 4. \quad (34)$$

The nonlinear weights are [6, 21]:

$$\omega_r = \frac{\alpha_r}{\sum_{s=0}^4 \alpha_s}, \quad \alpha_r = \frac{d_r}{(\epsilon + \beta_r)}, \quad r = 0, \dots, 4, \quad (35)$$

with

$$d_r = \Delta \eta^{4-r}, \quad \text{for } r = 0, \dots, 3, \quad d_4 = 1 - \sum_{r=0}^3 d_r, \quad (36)$$

and $\epsilon = 10^{-6}$.

The smoothness indicators are computed with $r = 1, \dots, 4$, [5]:

$$\beta_0 = \Delta \eta^2, \quad (37)$$

$$\beta_r = \sum_{l=1}^r \Delta \eta^{2l-1} \int_{\eta_0 - \Delta \eta/2}^{\eta_0 + \Delta \eta/2} \left(\frac{d^l}{d\eta^l} p_r(\eta) \right)^2 d\eta. \quad (38)$$

The 1D WENO-type extrapolation is then given by

$$\left\{ \partial_\eta^{(l)} p(\eta) \right\}_{l=0}^4 = \sum_{r=0}^4 \omega_r \frac{d^l}{d\eta^l} p_r(\eta). \quad (39)$$

Now, suppose we want to impose boundary conditions at $\eta_0 = (x_0, y_0)$ at the wall, presented in Figure 1.

For the Navier–Stokes equations, we are interested in two situations: known wall temperature and heat flux. At the wall, the normal velocity component is zero and, because of the non-slip condition, the tangent velocity component will match the wall velocity.

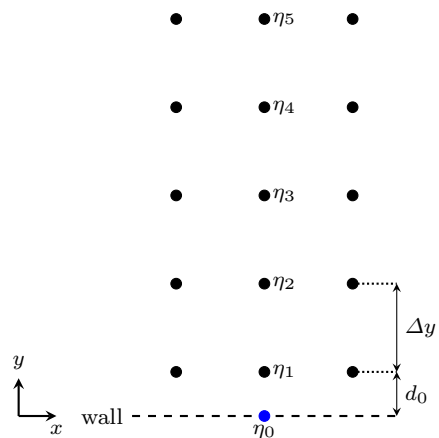


Fig. 1: Region near a wall.

2.2.1 Known Wall Temperature

For a known wall temperature, we can write

$$p = \rho R T_{\text{wall}}, \quad v = v_{\text{wall}}, \quad u = u_{\text{wall}}, \quad (40)$$

where R is the gas constant.

We now adapt the ILW procedure of [5] to impose the boundary conditions regarding [2, 22]. We let the detailed algebra for the Appendix and rewrite (1) as

$$U_t + \mathbf{F}(\mathbf{U})_x + \mathbf{G}'(\mathbf{U})\mathbf{U}_y = \boldsymbol{\Psi}_1 \mathbf{U}_{xx} + \boldsymbol{\Psi}_2 \mathbf{U}_{yy} + \boldsymbol{\Psi}_3 \mathbf{U}_{xy} + \mathbf{N}. \quad (41)$$

It is advisable to consider the general convection-diffusion case because it is a combination of both phenomena. For that, we can use a convex combination where each contribution can be adjusted via previously defined parameters [2]. We diagonalize the matrices in front of the first and second y -direction derivatives and write

$$\mathbf{V} = \mathbf{L}\mathbf{U}, \quad \mathbf{A} = \text{diag}(v - a, v, v, v + a), \quad (42)$$

$$\mathbf{V}_d = \mathbf{L}_d \mathbf{U}, \quad \mathbf{A}_d = \text{diag}\left(0, \frac{\mu}{\rho}, \frac{4\mu}{3\rho}, \frac{\gamma\mu}{Pr\rho}\right), \quad (43)$$

where the subscript d denotes “diffusive”. One may refer to the Appendix for the diffusive eigenvectors.

If we use (43) to rewrite (41) we will also be able to get a scalar hyperbolic equation and a parabolic system,

as in [2]. Therefore, the same conclusions apply. As in [2], we can write

$$\mathbf{B} = \mathbf{L}_d \mathbf{G}'(\mathbf{U}) \mathbf{R}_d = \begin{bmatrix} v & 0 & -\frac{a}{\gamma} & 0 \\ 0 & v & 0 & 0 \\ -a & 0 & v & -a \\ 0 & 0 & -\frac{a}{\gamma}(\gamma - 1) & v \end{bmatrix}. \quad (44)$$

We also define [2]

$$b_1 = (B_{11}^2 + B_{12}^2 + B_{13}^2 + B_{14}^2) \Delta x^2, \quad (45)$$

$$\epsilon_1 = 3(\lambda_{d2}^2 + \lambda_{d3}^2 + \lambda_{d4}^2), \alpha_1 = \frac{b_1}{b_1 + \epsilon_1}$$

$$b_2 = \frac{1}{3} (a_1 + a_3 + a_4), \quad (46)$$

$$\epsilon_2 = 9\lambda_{d2}^2, \alpha_2 = \frac{b_2}{b_2 + \epsilon_2},$$

$$b_3 = (B_{31}^2 + B_{32}^2 + B_{33}^2 + B_{34}^2) \Delta x^2, \quad (47)$$

$$\epsilon_3 = 9\lambda_{d3}^2, \alpha_3 = \frac{b_3}{b_3 + \epsilon_3},$$

$$b_4 = (B_{41}^2 + B_{42}^2 + B_{43}^2 + B_{44}^2) \Delta x^2, \quad (48)$$

$$\epsilon_4 = 9\lambda_{d4}^2, \alpha_4 = \frac{b_4}{b_4 + \epsilon_4}.$$

With α_m , $m = 1, \dots, 4$, and $k = 0, \dots, 4$, we have the following convex combination of convection and diffusion terms [2]

$$\partial_y^{(k)}(V_m)_{cc} = \alpha_m \partial_y^{(k)}(V_m)_c + (1 - \alpha_m) \partial_y^{(k)}(V_m)_d. \quad (49)$$

We now discuss how convection and diffusion terms are obtained. Starting with $\partial_y^{(k)} \mathbf{V}_c$, we assess the eigenvalues signs and the direction. Regarding Figure 1, $\lambda_1 < 0$, $\lambda_{2,3} \approx 0$, and $\lambda_4 > 0$. Therefore, we must impose the boundary conditions on the fourth characteristic variable. To form the eigensystem, $\partial_y^{(0)} U_1$ is approximated at the boundary with the WENO-type extrapolation and

$$(U_1)_{\eta_0} = \partial_y^{(0)} U_1, \quad (U_2)_{\eta_0} = u_{\text{wall}} \partial_y^{(0)} U_1, \quad (50)$$

$$(U_3)_{\eta_0} = v_{\text{wall}} \partial_y^{(0)} U_1,$$

$$(U_4)_{\eta_0} = \frac{\partial_y^{(0)} U_1 RT_{\text{wall}}}{\gamma - 1} + \frac{\partial_y^{(0)} U_1}{2} (u_{\text{wall}}^2 + v_{\text{wall}}^2).$$

With \mathbf{U}_{η_0} , we compute \mathbf{R} , \mathbf{A} , and \mathbf{L} . Next, we do a local characteristic decomposition on $S_a = \{\eta_1, \eta_2, \eta_3, \eta_4, \eta_5\}$

$$\mathbf{V} = \mathbf{L} \mathbf{U}, \quad (51)$$

and use the WENO-type extrapolation to obtain $\{\partial_y^{(l)} \mathbf{V}\}_{l=0}^4$ at the boundary.

We remark that if the S_a points are outside the computational domain, one can use the least squares

strategy with WENO-type extrapolation to approximate them. Details of this strategy will be presented next.

We first update $\partial_y^{(0)}(U_1)$ with

$$\partial_y^{(0)}(V_1) = \partial_y^{(0)}(U_1) \left[l_{11} + u_{\text{wall}} l_{12} + v_{\text{wall}} l_{13} + l_{14} \left(\frac{RT_{\text{wall}}}{\gamma - 1} + \frac{u_{\text{wall}}^2 + v_{\text{wall}}^2}{2} \right) \right]. \quad (52)$$

Then,

$$\partial_y^{(0)}(U_2) = u_{\text{wall}} \partial_y^{(0)}(U_1), \quad \partial_y^{(0)}(U_3) = v_{\text{wall}} \partial_y^{(0)}(U_1),$$

$$\partial_y^{(0)}(U_4) = \frac{\partial_y^{(0)}(U_1) RT_{\text{wall}}}{\gamma - 1} + \frac{\partial_y^{(0)}(U_1)}{2} (u_{\text{wall}}^2 + v_{\text{wall}}^2). \quad (53)$$

With the ILW, we update

$$\partial_y^{(1)} V_4 = \frac{-(F_1)_x + (S_{11})_x + \partial_y^{(1)} S_{21}}{r_{14}(v_{\text{wall}} + a)} - \frac{r_{11}(v_{\text{wall}} - a) \partial_y^{(1)} V_1 - r_{12} v_{\text{wall}} \partial_y^{(1)} V_2 - r_{13} v_{\text{wall}} \partial_y^{(1)} V_3}{r_{14}(v_{\text{wall}} + a)}. \quad (54)$$

With $\partial_y^{(k)} \mathbf{V}$, the conservative variable derivatives are

$$\{\partial_y^{(l)} \mathbf{U}\}_{l=1}^4 = \mathbf{R} \{\partial_y^{(l)} \mathbf{V}\}_{l=1}^4. \quad (55)$$

Then,

$$\{\partial_y^{(l)} \mathbf{V}_c\}_{l=0}^4 = \mathbf{L}_d \{\partial_y^{(l)} \mathbf{U}\}_{l=0}^4, \quad (56)$$

where \mathbf{R}_d , \mathbf{A}_d , and \mathbf{L}_d are also obtained with \mathbf{U}_{η_0} .

As one can see in (54), approximations to the x -direction inviscid flux and viscous terms first derivatives are needed. We now address how to obtain high-order approximations to the derivatives, matrices, nonlinear terms, fluxes, and viscous terms. We remark that \mathbf{U}_t are part of the known boundary conditions, which in this work are zero because the flows are steady.

We have \mathbf{U} in the vicinity of η_0 and we use it to obtain 2D least square polynomials, P_r , with $r = 1, \dots, 4$. One should notice that the polynomial must be obtained for each \mathbf{U} component separately. To compute P_r , we follow the procedure of [22], i.e., we start with the nearest $(r+1)^2$ interior points to η_0 and add points if the matrix rank is deficient. After obtaining the polynomials, we approximate \mathbf{U}_x , \mathbf{U}_y , and \mathbf{U}_{xx} on S_a in different substencils [5].

For instance, for one \mathbf{U}_x component

$$S_0 = \{0\}, \quad S_1 = \{P_1(\eta_1)_x, P_1(\eta_2)_x\}, \quad (57)$$

$$S_2 = \{P_2(\eta_1)_x, P_2(\eta_2)_x, P_2(\eta_3)_x\}, \quad (58)$$

$$S_3 = \{P_3(\eta_1)_x, P_3(\eta_2)_x, P_3(\eta_3)_x, P_3(\eta_4)_x\}, \quad (59)$$

$$S_4 = \{P_4(\eta_1)_x, P_4(\eta_2)_x, P_4(\eta_3)_x, P_4(\eta_4)_x, P_4(\eta_5)_x\}. \quad (60)$$

With \mathbf{U} and \mathbf{U}_x , we compute $\mathbf{F}(\mathbf{U})_x$ on those different substencils. Then, we use the WENO-type extrapolation to approximate $\partial_y^{(0)} \mathbf{F}(\mathbf{U})_x$ at η_0 . For the y -direction flux, we compute $\mathbf{G}(\mathbf{U})$ on S_a and approximate $\{\partial_y^{(l)} \mathbf{G}(\mathbf{U})\}_{l=0}^4$ with the WENO-type extrapolation. With similar ideas, $\{\partial_y^{(l)} \mathbf{U}_x\}_{l=0}^1$ and $\partial_y^{(0)} \mathbf{U}_{xx}$ are also approximated at η_0 .

Ψ_1 , Ψ_2 , Ψ_3 , and other matrices for the diffusive terms are obtained with the approximated derivatives and $\partial_y^{(0)} \mathbf{U}$, i.e., with WENO-type extrapolation. The nonlinear terms can now be computed with the Appendix formulae. Then,

$$\mathbf{S}_{1x} = \boldsymbol{\psi}_1 \frac{\partial \mathbf{W}}{\partial \mathbf{U}} \partial_y^{(1)} \mathbf{U}_x + \boldsymbol{\psi}_2 \frac{\partial \mathbf{W}}{\partial \mathbf{U}} \partial_y^{(0)} \mathbf{U}_{xx} + \mathbf{N}_1. \quad (61)$$

Finally, we compute \mathbf{S}_2 on S_a with

$$\mathbf{W}_x = \frac{\partial \mathbf{W}}{\partial \mathbf{U}} \mathbf{U}_x, \quad \mathbf{W}_y = \frac{\partial \mathbf{W}}{\partial \mathbf{U}} \mathbf{U}_y, \quad (62)$$

and approximate $\{\partial_y^{(l)} \mathbf{S}_2\}_{l=0}^4$ at η_0 with the WENO-type extrapolation.

For the diffusive terms, we also perform a decomposition on S_a

$$\mathbf{V}_d = \mathbf{L}_d \mathbf{U}, \quad (63)$$

and use the WENO-type extrapolation to obtain $\{\partial_y^{(l)} \mathbf{V}_d\}_{l=0}^4$ at the boundary.

As stated in [2], the number of boundary conditions depends on the normal velocity sign and the coordinate direction. In our case, a positive velocity v is oriented towards the computational domain. Therefore, for $v > 0$ we shall impose four boundary conditions and three for $v \leq 0$.

Particularly, if the wall is not moving both velocities are zero ($u_{\text{wall}} = v_{\text{wall}} = 0$) regardless of its inclination. Therefore, we only need to impose three boundary conditions and the local coordinate system and transformation of the equations are not required. This is advantageous because the number of least squares approximations is reduced, as discussed in [22]. Then, the conservative variables at the boundary can be updated

with

$$\begin{aligned} \partial_y^{(0)}(V_1)_d &= \partial_y^{(0)}(U_1)_d \left[l_{d11} + u_{\text{wall}} l_{d12} + \right. \\ &\quad \left. v_{\text{wall}} l_{d13} + l_{d14} \left(\frac{RT_{\text{wall}}}{\gamma - 1} + \frac{u_{\text{wall}}^2 + v_{\text{wall}}^2}{2} \right) \right], \\ \partial_y^{(0)}(U_2)_d &= \partial_y^{(0)}(U_1)_d u_{\text{wall}}, \\ \partial_y^{(0)}(U_3)_d &= \partial_y^{(0)}(U_1)_d v_{\text{wall}}, \\ \partial_y^{(0)}(U_4)_d &= \partial_y^{(0)}(U_1)_d \left(\frac{RT_{\text{wall}}}{\gamma - 1} + \frac{u_{\text{wall}}^2 + v_{\text{wall}}^2}{2} \right). \end{aligned} \quad (64)$$

For stability, we compute

$$\begin{aligned} \partial_y^{(0)}(V_m)_d &= l_{dm1} \partial_y^{(0)} U_1 + l_{dm2} \partial_y^{(0)} U_2 + \\ &\quad l_{dm3} \partial_y^{(0)} U_3 + l_{dm4} \partial_y^{(0)} U_4, \quad m = 2, 3, 4. \end{aligned} \quad (65)$$

Then, we perform slightly modifications on the WENO-type extrapolation and its polynomials, and use the stencil $S_b = \{\eta_0, \eta_1, \eta_2, \eta_3, \eta_4\}$ to compute $\{\partial_y^{(l)}(V_d)_m\}_{l=0}^4$ for $m = 2, 3, 4$ at the boundary. One should notice that S_b have four substencils and the first one have two points, η_0 and η_1 . Now, $d_r = \Delta x^{4-r}$ for $r = 0, \dots, 2$, $d_3 = 1 - \sum_{r=0}^2 d_r$, and the formulae should be adjusted accordingly.

As in [2], we compute

$$\begin{aligned} l_{d1} \partial_y^{(2)} \mathbf{U}_d &= \partial_y^{(2)} V_{1d}, \\ \Psi_m \partial_y^{(2)} \mathbf{U}_d &= (U_m)_t + F_m(\mathbf{U})_x + \partial_y^{(1)} G_m(\mathbf{U}) - \\ &\quad \Psi_{1m} \mathbf{U}_{xx} - \Psi_{3m} \mathbf{U}_{xy} - N_m, \quad m = 2, 3, 4, \end{aligned} \quad (66)$$

which forms a 4×4 linear system with $\partial_y^{(2)} \mathbf{U}_d$ as unknowns.

Then, we update

$$\partial_y^{(2)} \mathbf{V}_d = \mathbf{L}_d \partial_y^{(2)} \mathbf{U}_d, \quad (67)$$

and the computation of diffusive terms is finished.

We now return to the convex combination. α_m is computed with \mathbf{U}_{η_0} and $\{\partial_y^{(l)}(V_m)_{cc}\}_{l=0}^4$ is obtained with (49). Then,

$$\{\partial_y^{(l)} \mathbf{U}\}_{l=0}^4 = \mathbf{R}_d \{\partial_y^{(l)} \mathbf{V}_{cc}\}_{l=0}^4. \quad (68)$$

We update the convective flux with

$$\partial_y^{(0)} \mathbf{G}(\mathbf{U}) = \mathbf{G}(\partial_y^{(0)} \mathbf{U}), \quad (69)$$

$$\partial_y^{(1)} \mathbf{G}(\mathbf{U}) = \mathbf{G}'(\mathbf{U}) \partial_y^{(1)} \mathbf{U}, \quad (70)$$

$$\partial_y^{(2)} \mathbf{G}(\mathbf{U}) = \frac{\partial^2}{\partial y^2} \mathbf{G}(\mathbf{U}). \quad (71)$$

We also update $\partial_y^{(0)} \mathbf{S}_2$ with

$$\mathbf{W}_x = \frac{\partial \mathbf{W}}{\partial \mathbf{U}} \partial_y^{(0)} \mathbf{U}_x, \quad \mathbf{W}_y = \frac{\partial \mathbf{W}}{\partial \mathbf{U}} \partial_y^{(1)} \mathbf{U}, \quad (72)$$

and then we update ψ_3 , ψ_4 , \mathbf{N}_2 using (A.7), (A.8), and (A.16) (see the Appendix). Then, we get

$$\partial_y^{(1)} \mathbf{S}_2 = \psi_3 \frac{\partial \mathbf{W}}{\partial \mathbf{U}} \partial_y^{(1)} \mathbf{U}_x + \psi_4 \frac{\partial \mathbf{W}}{\partial \mathbf{U}} \partial_y^{(2)} \mathbf{U} + \mathbf{N}_2. \quad (73)$$

At the ghost points, the interior scheme requires \mathbf{U} , $\mathbf{G}(\mathbf{U})$, and \mathbf{S}_2 . Therefore we use Taylor expansion to approximate them, e.g.,

$$\mathbf{U}_j = \sum_{l=0}^4 \frac{(y_j - y_0)^l}{l!} \partial_y^{(l)} \mathbf{U}. \quad (74)$$

2.2.2 Known Heat Flux

Regarding y is the normal direction in Figure 1, we now show how to handle a known heat flux at the wall. We change how the WENO-type extrapolation polynomials are obtained, now they must satisfy $p_r(\eta_j) = T(\eta_j)$ for $j = 1 \dots, r$, and

$$\frac{dp_r(y)}{dy} \Big|_{\eta_0} = \frac{\partial T}{\partial y} \Big|_{\eta_0} \quad r = 1, \dots, 4. \quad (75)$$

With T_{wall} , we use the procedure for known temperature of Section 2.2.1.

3 Numerical Problems

3.1 Simple 2D Flows

For the first simple 2D flow, we propose an analytical solution with non-constant viscosity similar to the Example 6 of [2]

$$\begin{aligned} \rho(x, y) &= \exp(\sin(x) \sin(y)), \\ u(x, y) &= 2 + 0.02(x^2 - \pi^2), \\ v(x, y) &= 1 + 0.01(y^2 - \pi^2), \quad p(x, y) = 5. \end{aligned} \quad (76)$$

In CFD, it is common to model the viscosity with temperature, e.g., Shutherland law. Since pressure is constant in this flow, we use

$$\mu = \frac{5 \times 10^{-5}}{\rho}. \quad (77)$$

By inserting the analytical solution into the Euler ($\mathbf{S}_1(\mathbf{U}) = \mathbf{S}_2(\mathbf{U}) = \mathbf{0}$) or Navier–Stokes equations, we compute the source terms, $\mathbf{S}(\mathbf{U})$, so the equations are analytically satisfied. We use $[-\pi, \pi] \times [-\pi, \pi]$ as domain and the analytical solution to compute the ghost points.

Our principal goal in solving this simple 2D flow is to test the methodology for Euler and Navier–Stokes equations. The observed accuracy orders of the Euler and Navier–Stokes solutions were similar; as such, for brevity we only present the accuracy results for the

Navier–Stokes in Table 1, where one can see that fifth order is being reached.

We now change the analytical solution to test the Navier–Stokes wall boundary treatment. As in [17], a compressible Couette flow is set with

$$\begin{aligned} u &= \frac{u_u}{A} y, \quad v = 0, \quad p = 5, \\ e &= e_l + \frac{y}{A} (e_u - e_l) + \frac{u_u^2 Pr}{2\gamma} \frac{y}{A} \left(1 - \frac{y}{A}\right), \\ \rho &= \frac{p}{e(\gamma - 1)}, \quad \rho_u = 1, \quad \rho_l = 1.25, \quad M_u = 0.3, \end{aligned} \quad (78)$$

where $M = \sqrt{u^2 + v^2}/a$ is the Mach number, the subscripts u and l means upper and lower, the domain is $[0, 0] \times [2, A]$, and the height A is set to 1 for simplicity.

One should notice that v is zero everywhere, $u = 0$ at the lower boundary, and $u \neq 0$ at the upper boundary. Therefore, we can approximate fixed and moving walls at those boundaries. Since the analytical solution is available, we use it at the left and right ghost points and focus on known wall temperature and heat flux boundary treatments. The accuracy tests are shown in Tables 2 and 3, where each situation is tested separately.

Despite being nonrealistic, the simple 2D flows are useful to show that the Navier–Stokes wall boundary treatment is high-order. We remark that the convex combination parameter suggest a convective dominant problem, $\min_m(\alpha_m) > 0.999$ for the most refined mesh.

We now arbitrarily set $Pr = 0.1$ and $\mu = 0.01$ to test the convex combination in an idealized mixed convective-diffusive problem, in which we only consider that the temperature is known at the lower boundary. The accuracy tests are shown in Table 4, where we can see that the Navier–Stokes wall boundary treatment is high-order.

3.2 Vortex Flow

We now start to test the methodology in idealized flows with nontrivial phenomena. For the vortex flow, we use (1) with $\mathbf{S} = \mathbf{0}$. We consider a stationary version of the idealized and isentropic vortex of [23]. Starting with $\rho = p = 1$ and $u = v = 0$, we add perturbations in (u, v) and in the temperature, $T = p/\rho$, [23]

$$\begin{aligned} (\delta u, \delta v) &= \frac{\epsilon}{2\pi} e^{0.5(1-r^2)} (-\bar{y}, \bar{x}), \\ \delta T &= -\frac{(\gamma - 1)\epsilon^2}{8\gamma\pi^2} e^{1-r^2}, \quad \delta s = 0, \end{aligned} \quad (79)$$

where $(\bar{x}, \bar{y}) = (x - 5, y - 5)$, $r^2 = \bar{x}^2 + \bar{y}^2$, the vortex strength is $\epsilon = 5$, and the entropy, $s = p/\rho^\gamma$, remains

Table 1: Density accuracy results for the Navier–Stokes simple 2D flow.

$\Delta x = \Delta y$	L^1 norm	Order	L^2 norm	Order	L^∞ norm	Order
$2\pi/10$	$2.47E + 00$	—	$5.34E - 01$	—	$2.38E - 01$	—
$2\pi/20$	$1.48E - 01$	4.06	$3.51E - 02$	3.93	$2.09E - 02$	3.51
$2\pi/40$	$4.33E - 03$	5.10	$1.05E - 03$	5.07	$7.31E - 04$	4.84
$2\pi/80$	$1.29E - 04$	5.07	$3.04E - 05$	5.11	$2.16E - 05$	5.08
$2\pi/160$	$4.09E - 06$	4.98	$9.69E - 07$	4.97	$7.38E - 07$	4.87

Table 2: Density accuracy results for the Navier–Stokes wall boundary treatment with known temperature.

$\Delta x = \Delta y$	L^1 norm	Order	L^2 norm	Order	L^∞ norm	Order
$2/10$	$1.24E - 04$	—	$1.34E - 04$	—	$2.32E - 04$	—
$2/20$	$1.05E - 05$	3.57	$1.39E - 05$	3.27	$3.68E - 05$	2.65
$2/40$	$6.46E - 07$	4.02	$1.09E - 06$	3.68	$3.59E - 06$	3.36
$2/80$	$2.01E - 08$	5.01	$3.70E - 08$	4.88	$1.20E - 07$	4.91
$2/160$	$1.92E - 10$	6.71	$3.83E - 10$	6.59	$2.85E - 09$	5.39

Table 3: Density accuracy results for the Navier–Stokes wall boundary treatment with known heat flux.

$\Delta x = \Delta y$	L^1 norm	Order	L^2 norm	Order	L^∞ norm	Order
$2/10$	$2.16E - 04$	—	$2.62E - 04$	—	$6.05E - 04$	—
$2/20$	$1.34E - 05$	4.02	$2.12E - 05$	3.63	$6.79E - 05$	3.15
$2/40$	$8.84E - 07$	3.92	$1.76E - 06$	3.60	$7.45E - 06$	3.19
$2/80$	$4.43E - 08$	4.32	$1.06E - 07$	4.05	$5.36E - 07$	3.80
$2/160$	$9.76E - 10$	5.50	$2.86E - 09$	5.21	$1.58E - 08$	5.08

Table 4: Density accuracy results for the mixed problem Navier–Stokes wall boundary treatment.

$\Delta x = \Delta y$	L^1 norm	Order	L^2 norm	Order	L^∞ norm	Order
$2/10$	$2.55E - 05$	—	$1.97E - 05$	—	$3.37E - 05$	—
$2/20$	$1.10E - 06$	4.54	$7.92E - 07$	4.64	$9.14E - 07$	5.20
$2/40$	$2.60E - 08$	5.40	$1.99E - 08$	5.31	$4.03E - 08$	4.50
$2/80$	$5.94E - 10$	5.45	$4.84E - 10$	5.36	$1.98E - 09$	4.35
$2/160$	$2.57E - 11$	4.53	$1.90E - 11$	4.67	$6.42E - 11$	4.94

undisturbed. We use the perturbed solution as the exact solution, $[0, 10] \times [0, 10]$ as domain, and periodic boundary conditions [23].

Although isentropic, the Euler vortex flow models recirculation, which is an important phenomenon that occurs in more complicated flows that do lack an analytical or exact solution. As stated in [25], care must be taken when solving the Euler vortex flow. For example, when using periodic boundary conditions one may have an infinite array of coupled interacting vortices [25]. We again are interested in accuracy tests, which are shown in Table 5.

For the Navier–Stokes vortex flow, the diffusion will prevent us to do the same accuracy tests. We present the Mach number color map for the Euler and Navier–Stokes in Figure 2, where we can see that they are visually similar.

3.3 Rayleigh–Taylor Instability

The next problem is the Rayleigh–Taylor instability, in which we use (1) with $\mathbf{S}(\mathbf{U}) = (0, 0, U_1, U_3)^T$ and as initial condition [7]

$$(\rho_0, p_0) = \begin{cases} (2, 2y + 1), & y < 1/2, \\ (1, y + 3/2), & y \geq 1/2, \end{cases} \quad (80)$$

$$u_0 = 0, \quad v_0 = -0.025a \cos(8\pi x). \quad (81)$$

The computational domain is $[0, 0.25] \times [0, 1]$, $t = 1.95$, and $\gamma = 5/3$ for this case only. We use constant values on the upper and lower boundaries, reflective boundary conditions on the left and right for the convective variables and inviscid fluxes [7], and periodic boundary conditions on the left and right for the viscous terms.

The Rayleigh–Taylor instability has a simple setup, and it is a shock-dominated problem with complicated flow structures. Although the exact solution is not available, it is a good test for symmetry. We present a color map for the density, and the 160×640 points mesh in

Table 5: Density accuracy results for the Euler vortex flow and $t = 1$.

$\Delta x = \Delta y$	L^1 norm	Order	L^2 norm	Order	L^∞ norm	Order
10/10	9.09E - 01	—	2.25E - 01	—	9.60E - 02	—
10/20	1.38E - 01	2.72	3.49E - 02	2.69	2.01E - 02	2.26
10/40	8.83E - 03	3.97	2.36E - 03	3.89	1.63E - 03	3.62
10/80	3.64E - 04	4.60	9.83E - 05	4.58	6.60E - 05	4.63
10/160	1.22E - 05	4.90	3.31E - 06	4.89	2.30E - 06	4.84

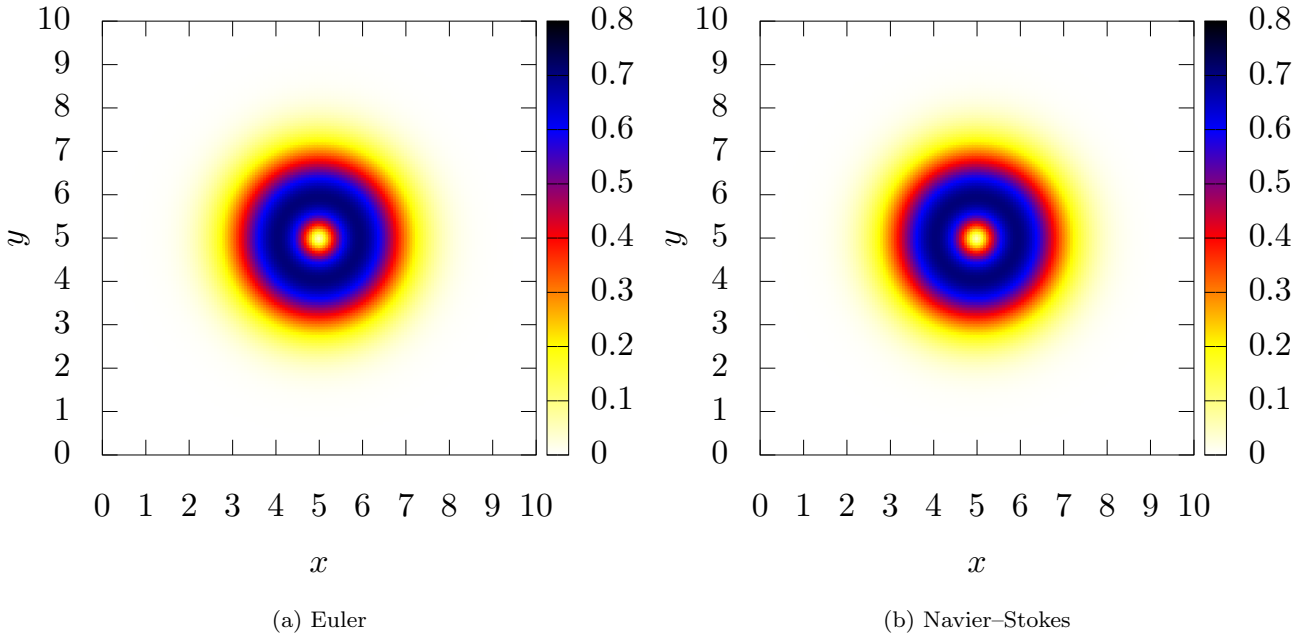
Fig. 2: Mach number color map for the vortex flow and 160×160 mesh.

Figure 3, where we can see a good representation of flow features for both Euler and Navier–Stokes, and that the latter seems to be more smooth, as expected. The L^1 , L^2 , and L^∞ norms of the difference of both sides of the symmetry line ($x = 0.125$) are presented in Table 6 for the 160×640 points mesh, where we can see an excellent hold of symmetry.

Table 6: L^1 , L^2 , and L^∞ norms of the difference of both sides of the symmetry line for the 160×640 points mesh.

Model	L^1 norm	L^2 norm	L^∞ norm
Euler	2.54E - 13	3.12E - 12	1.26E - 10
Navier–Stokes	1.18E - 15	9.97E - 15	2.69E - 13

3.4 Flow Past a Cylinder

We now turn our attention to the supersonic flow past a cylinder which radius is one and is centered at the origin. Similar to Example 7 of [2], we use as initial conditions

$$M(x, y) = \begin{cases} x^2 + y^2 - 1, & \text{if } 1 < x^2 + y^2 \leq 4, \\ 3, & \text{otherwise,} \end{cases} \quad (82)$$

$$\rho = \rho_0 \left(1 + \frac{\gamma - 1}{2} M^2 \right)^{-1/(\gamma-1)}, \quad (83)$$

$$p = p_0 \left(1 + \frac{\gamma - 1}{2} M^2 \right)^{-\gamma/(\gamma-1)}, \quad (84)$$

$$u = Ma, \quad v = 0, \quad (85)$$

with ρ_0 and p_0 computed with free-stream data $(\rho, u, v, p) = (1.4, 3, 0, 1)$.

For simplicity, we take $[-3, 6] \times [0, 6]$ as the domain and use the free-stream data at the upper, left, and

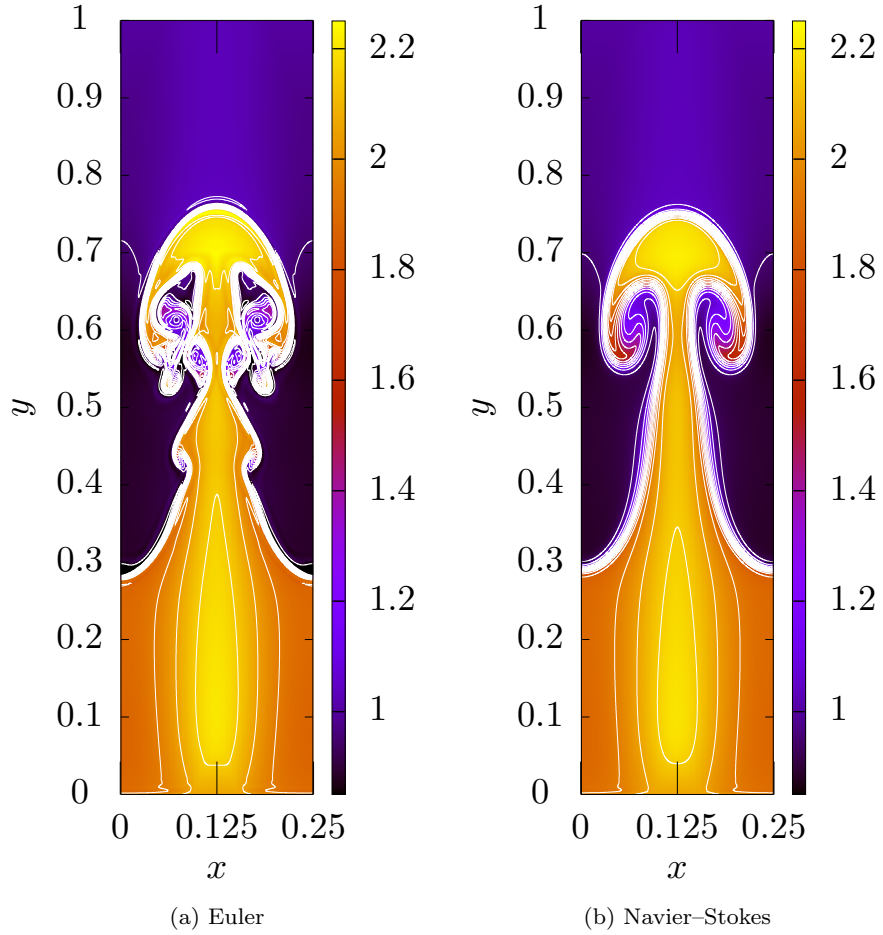


Fig. 3: Density color map for the Rayleigh–Taylor instability and 160×640 mesh with equally spaced contour lines from 0.85 to 2.25.

right ghost points of the domain. At $y = 0$ we use the symmetry condition and, at the walls, the ILW solid wall boundary treatment for the Navier–Stokes equations. The wall is fixed, $u_{\text{wall}} = v_{\text{wall}} = 0$, and $T_{\text{wall}} = T_0 = 2$.

The flow past a cylinder has an oblique shock near its walls, providing a good test case for the wall boundary treatment. We show the pressure color map and contours in Figure 4, where we can see that the oblique shock is being captured. We show six pressure profiles along constant y lines in Figure 5. Therefore, we conclude that the post-shock behavior is due to the contour lines generation.

For comparison, we also present the pressure profile along the center line for our results and the pressure profiles of [2] in Figure 6, where we can see that our result behaves similarly.

4 Concluding Remarks

Challenging engineering problems such as stall in aero-dynamic profiles or turbomachinery blades, flow separation, side loads, mixing, combustion, detonation, and turbulence demands robust numerical methods. To properly capture the flow phenomena, the Navier–Stokes equations are required.

We reviewed the well-established methods to solve the Euler equations and added the Navier–Stokes viscous terms discretization. Since the conservative variables first derivatives are available from the inviscid flux discretization, we computed the viscous terms, \mathbf{S}_1 and \mathbf{S}_2 , and employed a central fourth-order scheme to approximate its derivatives and finish the spatial discretization. To maintain the high-resolution of the interior scheme, we adapted the ILW boundary treatment of [2] regarding [22,5].

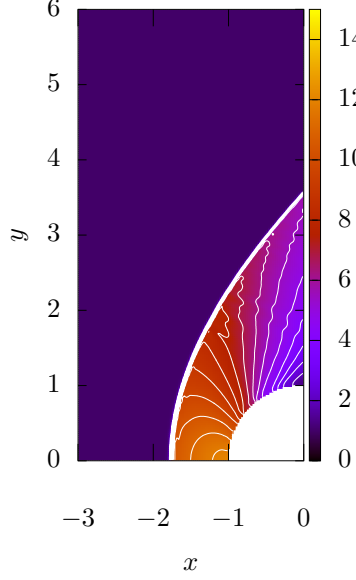


Fig. 4: Pressure color map for the flow past a cylinder and mesh with $\Delta x = \Delta y = 1/40$ and equally spaced contour lines from 2 to 15.

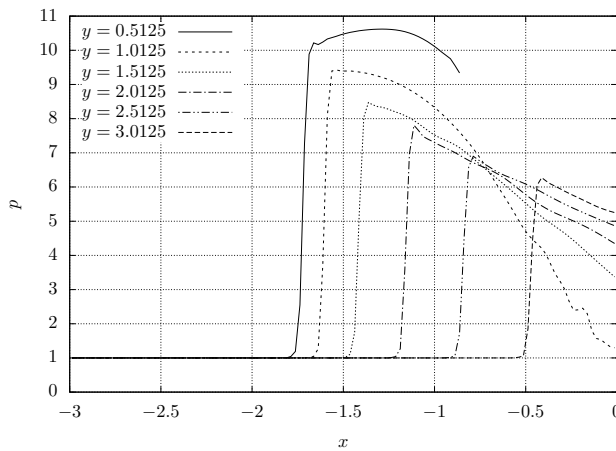


Fig. 5: Pressure profiles along constant y lines.

We showed that the proposed discretization can handle non-constant viscosity, has an excellent hold of symmetry, and, with the boundary treatment, is high-order and high-resolution. We remark that no approximations regarding the boundary layer were made, i.e., the methodology presented here could be considered for direct numerical simulations.

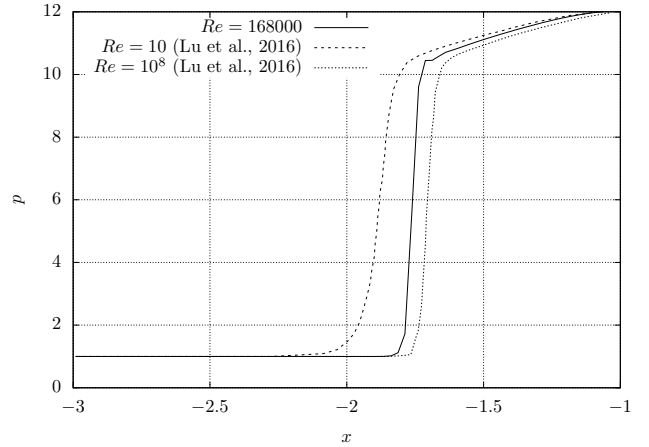


Fig. 6: Pressure profiles along the center line for the flow past a cylinder and meshes with $\Delta x = \Delta y = 1/40$ of [2] and this work.

Acknowledgements

We would like to thank Dr. Jianfang Lu from South China Normal University for valuable discussions and comments.

Conflict of interest

The authors declare that they have no conflict of interest.

Appendix. Matrices and Vectors for the Rewritten Navier–Stokes Equations

To rewrite the Navier–Stokes equations, we start expanding \mathbf{S}_1 and \mathbf{S}_2

$$\begin{aligned}
 (S_{1x})_1 &= 0, \\
 (S_{1x})_2 &= \mu_x \left(\frac{4}{3} u_x - \frac{2}{3} v_y \right) + \mu \left(\frac{4}{3} u_{xx} - \frac{2}{3} v_{xy} \right), \\
 (S_{1x})_3 &= \mu_x (u_y + v_x) + \mu (u_{xy} + v_{xx}), \\
 (S_{1x})_4 &= u_x \mu \left(\frac{4}{3} u_x - \frac{2}{3} v_y \right) + v_x \mu (u_y + v_x) + \\
 &\quad \left(\frac{\mu \gamma}{Pr(\gamma - 1)} \right)_x \left(\frac{p}{\rho} \right)_x + u \mu_x \left(\frac{4}{3} u_x - \frac{2}{3} v_y \right) + \\
 &\quad u \mu \left(\frac{4}{3} u_{xx} - \frac{2}{3} v_{xy} \right) + v \mu_x (u_y + v_x) + v \mu (u_{xy} + v_{xx}) + \\
 &\quad \frac{\mu \gamma}{Pr(\gamma - 1)} \left(\frac{p_{xx}}{\rho} + \frac{2p_x \rho_x^2}{\rho^3} - \frac{2p_x \rho_x}{\rho^2} - \frac{p \rho_{xx}}{\rho^2} \right), \tag{A.1}
 \end{aligned}$$

$$\begin{aligned}
(S_{2y})_1 &= 0, \\
(S_{2y})_2 &= \mu_y (u_y + v_x) + \mu (u_{yy} + v_{xy}), \\
(S_{2y})_3 &= \mu_y \left(\frac{4}{3} v_y - \frac{2}{3} u_x \right) + \mu \left(\frac{4}{3} v_{yy} - \frac{2}{3} u_{xy} \right), \\
(S_{2y})_4 &= u_y \mu (u_y + v_x) + v_y \mu \left(\frac{4}{3} v_y - \frac{2}{3} u_x \right) + \\
&\quad \left(\frac{\mu \gamma}{Pr(\gamma-1)} \right)_y \left(\frac{p}{\rho} \right)_y + u \mu_y (u_y + v_x) + \\
&\quad u \mu (u_{yy} + v_{xy}) + v \mu_y \left(\frac{4}{3} v_y - \frac{2}{3} u_x \right) + v \mu \left(\frac{4}{3} v_{yy} - \frac{2}{3} u_{xy} \right) \\
&\quad + \frac{\mu \gamma}{Pr(\gamma-1)} \left(\frac{p_{yy}}{\rho} + \frac{2p\rho_y^2}{\rho^3} - \frac{2p_y\rho_y}{\rho^2} - \frac{p\rho_{yy}}{\rho^2} \right). \tag{A.2}
\end{aligned}$$

One should notice that we did not consider μ and Pr as constants nor remove any terms. We now group terms containing first and second derivatives to the primitive variables, and nonlinear terms separately

$$\mathbf{S}_{1x} = \psi_1 \mathbf{W}_{xy} + \psi_2 \mathbf{W}_{xx} + \mathbf{N}_{w1}, \tag{A.3}$$

$$\mathbf{S}_{2y} = \psi_3 \mathbf{W}_{xy} + \psi_4 \mathbf{W}_{yy} + \mathbf{N}_{w2}, \tag{A.4}$$

where

$$\psi_1 = \begin{bmatrix} 0 & 0 & 0 & 0 \\ 0 & 0 & -2\mu/3 & 0 \\ 0 & \mu & 0 & 0 \\ 0 & \mu v & -2\mu u/3 & 0 \end{bmatrix}, \tag{A.5}$$

$$\psi_2 = \begin{bmatrix} 0 & 0 & 0 & 0 \\ 0 & 4\mu/3 & 0 & 0 \\ 0 & 0 & \mu & 0 \\ -\mu a^2/[\rho Pr(\gamma-1)] & 4\mu u/3 & \mu v & \mu \gamma/[\rho Pr(\gamma-1)] \end{bmatrix}, \tag{A.6}$$

$$\psi_3 = \begin{bmatrix} 0 & 0 & 0 & 0 \\ 0 & 0 & \mu & 0 \\ 0 & -2\mu/3 & 0 & 0 \\ 0 & -2\mu v/3 & \mu u & 0 \end{bmatrix}, \tag{A.7}$$

$$\psi_4 = \begin{bmatrix} 0 & 0 & 0 & 0 \\ 0 & \mu & 0 & 0 \\ 0 & 0 & 4\mu/3 & 0 \\ -\mu a^2/[\rho Pr(\gamma-1)] & \mu u & 4\mu v/3 & \mu \gamma/[\rho Pr(\gamma-1)] \end{bmatrix}, \tag{A.8}$$

$$\begin{aligned}
(N_{w1})_1 &= 0, \\
(N_{w1})_2 &= \mu_x \left(\frac{4}{3} u_x - \frac{2}{3} v_y \right), \\
(N_{w1})_3 &= \mu_x (u_y + v_x), \\
(N_{w1})_4 &= u_x \mu \left(\frac{4}{3} u_x - \frac{2}{3} v_y \right) + v_x \mu (u_y + v_x) + \\
&\quad \left(\frac{\mu \gamma}{Pr(\gamma-1)} \right)_x \left(\frac{p}{\rho} \right)_x + u \mu_x \left(\frac{4}{3} u_x - \frac{2}{3} v_y \right) + \\
&\quad v \mu_x (u_y + v_x) + \frac{\mu \gamma}{Pr(\gamma-1)} \left(\frac{2p\rho_x^2}{\rho^3} - \frac{2p_x\rho_x}{\rho^2} \right), \tag{A.9}
\end{aligned}$$

$$\begin{aligned}
(N_{w2})_1 &= 0, \\
(N_{w2})_2 &= \mu_y (u_y + v_x), \\
(N_{w2})_3 &= \mu_y \left(\frac{4}{3} v_y - \frac{2}{3} u_x \right), \\
(N_{w2})_4 &= u_y \mu (u_y + v_x) + v_y \mu \left(\frac{4}{3} v_y - \frac{2}{3} u_x \right) + \\
&\quad \left(\frac{\mu \gamma}{Pr(\gamma-1)} \right)_y \left(\frac{p}{\rho} \right)_y + u \mu_y (u_y + v_x) + \\
&\quad v \mu_y \left(\frac{4}{3} v_y - \frac{2}{3} u_x \right) + \frac{\mu \gamma}{Pr(\gamma-1)} \left(\frac{2p\rho_y^2}{\rho^3} - \frac{2p_y\rho_y}{\rho^2} \right). \tag{A.10}
\end{aligned}$$

The boundary treatment is based on conservative variables, we then transform to the latter with

$$\begin{aligned}
\mathbf{S}_{1x} &= \psi_1 \left[\mathbf{M} \mathbf{U}_y + \frac{\partial \mathbf{W}}{\partial \mathbf{U}} \mathbf{U}_{xy} \right] \\
&+ \psi_2 \left[\mathbf{M} \mathbf{U}_x + \frac{\partial \mathbf{W}}{\partial \mathbf{U}} \mathbf{U}_{xx} \right] + \mathbf{N}_{w1}, \tag{A.11}
\end{aligned}$$

$$\begin{aligned}
\mathbf{S}_{2y} &= \psi_3 \left[\mathbf{O} \mathbf{U}_x + \frac{\partial \mathbf{W}}{\partial \mathbf{U}} \mathbf{U}_{xy} \right] \\
&+ \psi_4 \left[\mathbf{O} \mathbf{U}_y + \frac{\partial \mathbf{W}}{\partial \mathbf{U}} \mathbf{U}_{yy} \right] + \mathbf{N}_{w2}, \tag{A.12}
\end{aligned}$$

$$\begin{aligned}
\mathbf{M} &= \begin{bmatrix} 0 & 0 & 0 & 0 \\ \frac{\rho_x u - \rho u_x}{\rho^2} & -\frac{\rho_x}{\rho^2} & 0 & 0 \\ \frac{\rho_x v - \rho v_x}{\rho^2} & 0 & -\frac{\rho_x}{\rho^2} & 0 \\ (uu_x + vv_x)(\gamma-1) - u_x(\gamma-1) & -v_x(\gamma-1) & 0 & 0 \end{bmatrix}, \\
\mathbf{O} &= \begin{bmatrix} 0 & 0 & 0 & 0 \\ \frac{\rho_y u - \rho u_y}{\rho^2} & -\frac{\rho_y}{\rho^2} & 0 & 0 \\ \frac{\rho_y v - \rho v_y}{\rho^2} & 0 & -\frac{\rho_y}{\rho^2} & 0 \\ (uu_y + vv_y)(\gamma-1) - u_y(\gamma-1) & -v_y(\gamma-1) & 0 & 0 \end{bmatrix}. \tag{A.13}
\end{aligned}$$

We finally write the viscous terms as

$$\mathbf{S}_{1x} = \psi_1 \frac{\partial \mathbf{W}}{\partial \mathbf{U}} \mathbf{U}_{xy} + \psi_2 \frac{\partial \mathbf{W}}{\partial \mathbf{U}} \mathbf{U}_{xx} + \mathbf{N}_1, \tag{A.14}$$

$$\mathbf{S}_{2y} = \psi_3 \frac{\partial \mathbf{W}}{\partial \mathbf{U}} \mathbf{U}_{xy} + \psi_4 \frac{\partial \mathbf{W}}{\partial \mathbf{U}} \mathbf{U}_{yy} + \mathbf{N}_2, \tag{A.15}$$

with

$$\begin{aligned}
\mathbf{N}_1 &= \psi_1 \mathbf{M} \mathbf{U}_y + \psi_2 \mathbf{M} \mathbf{U}_x + \mathbf{N}_{w1}, \\
\mathbf{N}_2 &= \psi_3 \mathbf{O} \mathbf{U}_x + \psi_4 \mathbf{O} \mathbf{U}_y + \mathbf{N}_{w2}. \tag{A.16}
\end{aligned}$$

Introducing four new terms, we write

$$\mathbf{S}_{1x} + \mathbf{S}_{2y} = \Psi_1 \mathbf{U}_{xx} + \Psi_2 \mathbf{U}_{yy} + \Psi_3 \mathbf{U}_{xy} + \mathbf{N} \tag{A.17}$$

with

$$\Psi_1 = \psi_2 \frac{\partial \mathbf{W}}{\partial \mathbf{U}}, \tag{A.18}$$

$$\Psi_2 = \psi_4 \frac{\partial \mathbf{W}}{\partial \mathbf{U}}, \tag{A.19}$$

$$\Psi_3 = \psi_1 \frac{\partial \mathbf{W}}{\partial \mathbf{U}} + \psi_3 \frac{\partial \mathbf{W}}{\partial \mathbf{U}}, \tag{A.20}$$

$$\mathbf{N} = \mathbf{N}_1 + \mathbf{N}_2. \tag{A.21}$$

To apply the wall boundary treatment, we need to diagonalize the matrix Ψ_2 . We choose the scaling factors in a way

that the resulting eigenvectors are similar to those employed in [2], i.e.,

$$\mathbf{L}_d = \begin{bmatrix} \frac{1}{2\gamma} & 0 & 0 & 0 \\ -u & 1 & 0 & 0 \\ \frac{v}{2a} & 0 & -\frac{1}{2a} & 0 \\ \frac{q(\gamma-1)}{2a^2} - \frac{1}{2\gamma} - \frac{u(\gamma-1)}{2a^2} - \frac{v(\gamma-1)}{2a^2} & \frac{\gamma-1}{2a^2} \end{bmatrix}, \quad (\text{A.22})$$

$$\mathbf{R}_d = \begin{bmatrix} 2\gamma & 0 & 0 & 0 \\ 2u\gamma & 1 & 0 & 0 \\ 2v\gamma & 0 & -2a & 0 \\ 2q\gamma + \frac{2a^2}{\gamma-1} & u - 2av & \frac{2a^2}{\gamma-1} \end{bmatrix}, \quad (\text{A.23})$$

with $q = (u^2 + v^2)/2$.

References

1. X. Zhang and C.-W. Shu, “Positivity-preserving high order finite difference WENO schemes for compressible Euler equations,” *Journal of Computational Physics*, vol. 231, no. 5, pp. 2245 – 2258, 2012.
2. J. Lu, J. Fang, S. Tan, C.-W. Shu, and M. Zhang, “Inverse Lax–Wendroff procedure for numerical boundary conditions of convection–diffusion equations,” *Journal of Computational Physics*, vol. 317, pp. 276 – 300, 2016.
3. N. Fleischmann, S. Adami, and N. A. Adams, “Numerical symmetry-preserving techniques for low-dissipation shock-capturing schemes,” *Computers & Fluids*, vol. 189, pp. 94 – 107, 2019.
4. J. Zhu and C.-W. Shu, “Convergence to steady-state solutions of the new type of high-order multi-resolution WENO schemes: a numerical study,” *Communications on Applied Mathematics and Computation*, Sept. 2019.
5. J. Lu, C.-W. Shu, S. Tan, and M. Zhang, “An inverse Lax–Wendroff procedure for hyperbolic conservation laws with changing wind direction on the boundary,” *Journal of Computational Physics*, p. 109940, 2020.
6. R. Borges, M. Carmona, B. Costa, and W. S. Don, “An improved weighted essentially non-oscillatory scheme for hyperbolic conservation laws,” *Journal of Computational Physics*, vol. 227, pp. 3191–3211, 2008.
7. F. Acker, R. B. de R. Borges, and B. Costa, “An improved WENO-Z scheme,” *Journal of Computational Physics*, vol. 313, pp. 726–753, 2016.
8. J. Zhu and C.-W. Shu, “A new type of multi-resolution WENO schemes with increasingly higher order of accuracy,” *Journal of Computational Physics*, vol. 375, pp. 659 – 683, 2018.
9. Z. Gao, W. S. Don, and Z. Li, “High order weighted essentially non-oscillation schemes for two-dimensional detonation wave simulations,” *Journal of Scientific Computing*, vol. 53, no. 1, pp. 80–101, 2012.
10. C. Zhu, J. Chen, J. Wu, and T. Wang, “Dynamic stall control of the wind turbine airfoil via single-row and double-row passive vortex generators,” *Energy*, vol. 189, p. 116272, 2019.
11. S. Verma, A. Hadjadj, and O. Haidn, “Origin of side-loads in a subscale truncated ideal contour nozzle,” *Aerospace Science and Technology*, vol. 71, pp. 725 – 732, 2017.
12. I. Ivanov and I. Kryukov, “Numerical study of ways to prevent side loads in an over-expanded rocket nozzles during the launch stage,” *Acta Astronautica*, vol. 163, pp. 196 – 201, 2019. Space Flight Safety-2018.
13. H. Wang, X. Jiang, Y. Chao, Q. Li, M. Li, W. Zheng, and T. Chen, “Effects of leading edge slat on flow separation and aerodynamic performance of wind turbine,” *Energy*, vol. 182, pp. 988 – 998, 2019.
14. M. Righi, V. Pachidis, and L. Könözsy, “On the prediction of the reverse flow and rotating stall characteristics of high-speed axial compressors using a three-dimensional through-flow code,” *Aerospace Science and Technology*, vol. 99, p. 105578, 2020.
15. H. Fatahian, H. Salarian, M. E. Nimvari, and J. Khaleghinia, “Computational fluid dynamics simulation of aerodynamic performance and flow separation by single element and slatted airfoils under rainfall conditions,” *Applied Mathematical Modelling*, vol. 83, pp. 683 – 702, 2020.
16. C. Lee, K. Choi, C. Kim, and S. Han, “Computational investigation of flow separation in a thrust-optimized parabolic nozzle during high-altitude testing,” *Computers & Fluids*, vol. 197, p. 104363, 2020.
17. C. Liang, S. Premasuthan, A. Jameson, and Z. J. Wang, *Large Eddy Simulation of Compressible Turbulent Channel Flow with Spectral Difference method*. 2009.
18. M. Atak, J. Larsson, G. Gassner, and C. dieter Munz, *DNS of a flat-plate supersonic boundary layer using the discontinuous Galerkin spectral element method*. 2014.
19. W. Rozema, R. W. C. P. Verstappen, A. E. P. Veldman, and J. C. Kok, “Low-dissipation simulation methods and models for turbulent subsonic flow,” *Archives of Computational Methods in Engineering*, vol. 27, pp. 299–330, 2020.
20. J. Holgate, A. Skillen, T. Craft, and A. Revell, “A review of embedded large eddy simulation for internal flows,” *Archives of Computational Methods in Engineering*, vol. 26, pp. 865–882, 2019.
21. S. Tan, C. Wang, C.-W. Shu, and J. Ning, “Efficient implementation of high order inverse Lax–Wendroff boundary treatment for conservation laws,” *Journal of Computational Physics*, vol. 231, pp. 2510–2527, 2012.
22. R. B. de R. Borges, N. D. P. da Silva, F. A. A. Gomes, C.-W. Shu, and S. Tan, “A sequel of inverse Lax–Wendroff high order wall boundary treatment for conservation laws,” *Archives of Computational Methods in Engineering*, 2020.
23. C.-W. Shu, *Essentially non-oscillatory and weighted essentially non-oscillatory schemes for hyperbolic conservation laws*, pp. 325–432. Berlin, Heidelberg: Springer Berlin Heidelberg, 1998.
24. Z. Hong, Z. Ye, and K. Ye, “An improved weno-z scheme with symmetry-preserving mapping,” *Advances in Aerodynamics*, vol. 2, p. 18, Aug. 2020.
25. S. C. Spiegel, H. Huynh, and J. R. DeBonis, *A Survey of the Isentropic Euler Problem using High-Order Methods*. 2015.